Journal of Applied Electrochemistry (2005) 35:683–692
DOI 10.1007/s10800-005-1366-8


# The photoelectrocatalytic oxidation of aqueous nitrophenol using a novel reactor

P.A. CHRISTENSEN*, T.A. EGERTON, S.A.M. KOSA, J.R. TINLIN and K. SCOTT
*School of Chemical Engineering and Advanced Materials, Merz Court, The University, Newcastle upon Tyne, NE1 7RU, UK*
*(*author for correspondence, e-mail: p.a.christensen@ncl.ac.uk; tel/fax: +44-191 222 5472)*

Received 15 June 2004; accepted in revised form 16 November 2004

*Key words:* bubble column reactor, electric field enhancement, nitrophenol, photoelectrocatalytic, sol–gel $TiO_2$ electrode, thermal $TiO_2$ electrode

## Abstract

This paper reports the oxidation of aqueous 4-nitrophenol solutions in a photo-electrochemical bubble column reactor (BCR) in which mass transfer has been shown not to be rate limiting. The work represents the first steps in the scale-up of active photoanodes and efficient reactors for the disinfection and detoxification of water.

The preparation, optimization and application of two types of electrode are described and the results are compared with those for a $TiO_2$ electrode supplied by Ineos Chlor. Photocurrents measured in tap water and in aqueous methanol were used for the initial characterization of the electrodes. The methanol was employed for diagnostic purposes only, as discussed below; methanol can react either by direct hole transfer or by hydroxyl radical recombination, but the balance of these reactions depends upon the nature of the electrode surface. The most active thermal electrodes were fabricated by heating titanium metal in air at 750 °C for 10 min, whilst the most active sol–gel electrodes were heated at 600 °C for 10 min.

Three of the central achievements of the work were to: (1) show that it is possible to design and fabricate photoelectrochemical reactors capable of effecting the mineralization of strongly absorbing organics; (2) confirm that the photocatalytic decomposition of 4-NP in reactors with a 4 $dm^3$ capacity can be increased by the application of a small positive potential and (3) that the application of such a potential *significantly* enhances the *mineralization* of 4-NP.

For the mineralization of 0.25 mM nitrophenol solutions the reactivity sequence is:

Photoelectrocatalytic > Photocatalytic > Photochemical > Electrochemical.

However, even at 3 V applied potential, charge recombination is not eliminated. The order of electrode activity was:

Ineos > Sol Gel > Thermal.

Differences between the activities of different electrodes were attributed to changes in the structure and morphology of the $TiO_2$. It is noteworthy that although, for nitrophenol oxidation, the thermal electrodes were the least active, for photoelectrocatalytic disinfection in the same type of reactor, thermal electrodes were the most active.

## 1. Introduction

The photocatalytic properties of both anatase and rutile polymorphs of $TiO_2$ are well-attested in the literature [1–3]. UV generation of an electron–hole pair initiates the subsequent catalytic activity, and it is generally believed that the active oxidant at the surface of irradiated $TiO_2$ is the hydroxyl radical ($^{\bullet}OH$) which is only slightly less oxidizing than fluorine [2]. Although the photocatalytic activity of $TiO_2$ has been known for many years [4] the ability to generate $^{\bullet}OH$ radicals on irradiation with UV light of wavelength $> 350$ nm has been exploited for destruction of organics [5, 6] or for photocatalytic disinfection [7] only comparatively recently.

The papers referred to above describe the application of $TiO_2$ in the form of a powder added to contaminated water (i.e. as slurry), unfortunately, there are two significant problems associated with this approach:

(1) The $TiO_2$ must be removed from the treated water.
(2) The majority of the light energy is wasted as heat due to the recombination of the electron–hole pairs, thus the quantum efficiency for $^{\bullet}OH$ generation has been reported as being only ca. 4% [8].

The recognition of the practical problems of removing the $TiO_2$ from treated water has led to numerous attempts to immobilize the catalyst particles on a variety of substrates [9–12] including carbon [9] and glass fibre [10]. However, immobilization introduces its own potential problems; in particular, target molecules must diffuse much further to the catalyst surface if it is immobilized. An order of magnitude calculation suggests a diffusion distance of $10^2$–$10^3$ nm in an ideally dispersed 0.1 wt% slurry of 70 $m^2$ $g^{-1}$ $TiO_2$, and this is significantly less than the length scale of a few mm in a typical reactor with an immobilized catalyst.

As shown in Figure 1, providing that the electrolyte concentration exceeds the dopant density, the application of a positive potential to an n-type $TiO_2$ photoanode generates an electric field within the semiconductor [13–15]. The thickness $W$ of the depletion layer varies as [15] $(V-V_f)^{1/2}$ where $V$ is the potential at the conduction band edge, and $V_f$ is the flat band potential. Photons of sufficient energy to excite electrons across the band gap are absorbed to a depth $1/\alpha$ where $\alpha$ is the absorption coefficient of the incident light at the wavelength of interest. If $1/\alpha$ is less than $(W + L_p)$, where $L_p$ is the minority carrier length [14], separation of the charge carriers is enhanced by the potential gradient as holes are driven 'uphill' to the surface and electrons are swept towards the interior of the semiconductor, where they eventually reach the back contact and are driven around the external circuit by the applied potential difference to the counter electrode. Hence, in contrast to the situation in slurries, capture of photogenerated electrons is no longer rate limiting [16] even though charge-carriers generated at depths greater than $(W + L_p)$ will mostly recombine.

From the above discussion it may be seen that adherence to the relationship $J_p\alpha(V-V_f)^{1/2}$ constitutes a simple test of the classical theory. In contrast, the applicability of the simple theory to nanocrystalline materials is not necessarily straightforward; e.g. the crystal size may be too small to allow the depletion layer to develop fully. Therefore, we report the performance of two different nanocrystalline electrode types. The first, a 'thermal film', made by heating titanium metal in air [17–19] may be expected to approximate to the theory described above – the rutile crystal size in the optimum thermal electrodes is 50–70 nm. The second prepared by the deposition of nano-particles [17–19] is expected to have a very different morphology, and the X-ray line broadening measurements described below suggest that the anatase crystal size in the optimum electrodes is ~20 nm. Therefore, a comparison of the properties of the two electrodes highlights the contribution of electrode morphology to the observed photoelectrocatalytic behaviour. To ensure a sound basis of comparison, the preparation conditions leading to optimum performance were established by current–voltage measurements on small (1 cm × 1 cm) or (5 cm × 5 cm) electrodes of each type, after which larger scale electrodes were tested with respect to the photoelectrochemical oxidation of 4-nitrophenol (4-NP). We also tested a third $TiO_2$ electrode type, supplied by Ineos Chlor, in order to benchmark our electrodes against possible commercial suppliers.

Nitrophenol is a demanding choice with respect to photocatalytic oxidation because it is a large molecule, and hence a number of electron transfers are required to effect its mineralization. In addition, the oxidation of nitrophenol involves many potential intermediates, any one of which may be intractable. Although the degradation of 4-NP has been achieved photocatalytically using $TiO_2$ slurries [20], the strong UV absorption of 4-NP makes it a demanding target molecule for photocatalytic oxidation at an immobilized surface. A particular objective of this work was to establish whether practical photoelectrocatalytic reactors employing immobilized $TiO_2$ films could be realized for such strongly absorbing solutions.

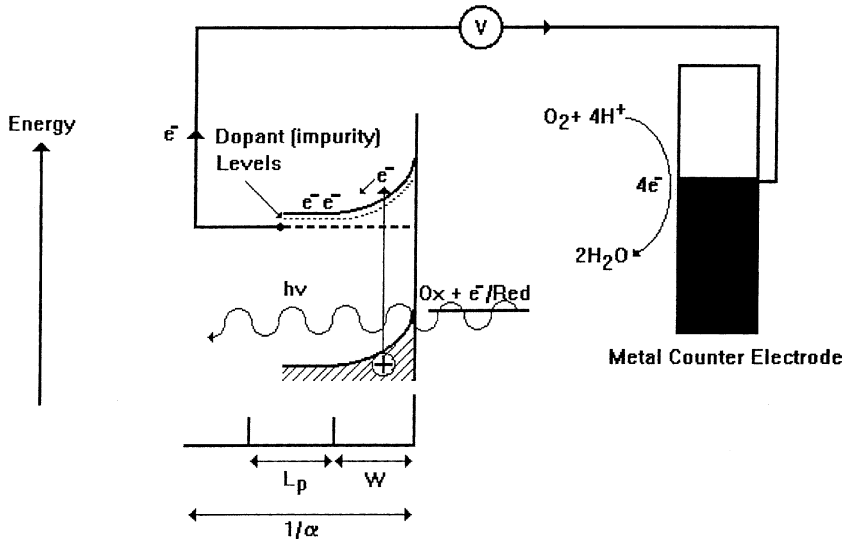


*Fig. 1.* Schematic representation of the electric field enhancement effect, see text for details.

## 2. Experimental

### 2.1. *Electrode preparation and characterization*

Results are reported for thermal and sol–gel films formed on Ti plates, either 1 cm × 1 cm × 0.1 cm or 5 cm × 5 cm × 0.3 cm (Goodfellow, 99.6 + %), or mesh 15 cm × 10 cm × 0.02 cm (Expanded Mesh Ltd), and for commercial Ineos Chlor electrodes. The thermal electrodes were formed by heating the plate or mesh in air at the required temperature for 10 min. The sol–gel electrodes were prepared by the method of O'Regan and colleagues [21]. The plate or mesh titanium substrates were dip-coated, spun at 2500 rpm and then heated at the required temperature for 10 min in air. The highest photocurrents were measured after five dip/spin/heat cycles and this procedure was used for all the sol–gel results reported below.

The electrodes were characterized, using a Sycopel AEW2 potentiostat interfaced to a PC, by the measurement of the cyclic voltammograms of the plate electrodes in a 250-$cm^3$ glass cylindrical cell [18], in which a Pt mesh counter electrode (90 mm diameter, 63% open area, Goodfellow) was mounted above the 1 (or 25) $cm^2$ $TiO_2$ photoanode. The Ag/AgCl wire reference electrode was checked regularly against a commercial Ag/AgCl reference electrode (Sentek). The $TiO_2$ electrodes were irradiated by 2 × 36 W Philips PL-L lamps ($\lambda_{max}$~360 nm) positioned horizontally above the cell.

The crystallinity of the 1-$cm^2$ $TiO_2$ electrode plates was determined from powder diffractograms (Philips Xpert X-ray diffractometer ($CuK_\alpha$ source)). Calibration curves were prepared by measuring the diffractograms of calibration standards made by mixing powders consisting of 100% anatase (Tioxide AHR) and (97% rutile + 3% anatase, Tioxide RFC5) and measuring the peak areas of the $2\theta = 25.28$ (anatase, (101)) and 27.45 (rutile, (110)) lines. Crystallite sizes were determined from the Debye–Scherrer equation [22].

### 2.2. *The photoelectrocatalytic reactor*

The ~1 $dm^3$ photoelectrocatalytic bubble column reactor (BCR), which was specifically designed for operation with strongly absorbing solutions such as 4-NP, was constructed from two concentric Pyrex™ tubes (inner tube: 42 mm external diameter, outer tube: 80 mm internal diameter). It was connected by non-absorbing silicone tubing (TYGON) to an external 3 $dm^3$ tank and NP solution was recirculated at ~$3 \times 10^{-5}$ $m^3$ $s^{-1}$, see Figures 2 and 3; a detailed description is given elsewhere [23], excellent mass transfer can be achieved in this reactor by gas-sparging with small bubbles generated by passing gas through a sintered glass distributor at its base. However, since control experiments demonstrated that mass transport was not rate-limiting in our photoelectrocatalytic experiments, gas sparging (5 $dm^3$ $min^{-1}$) was only employed in the studies using the P25 slurry (Degussa) in order to maintain the $TiO_2$ particles in suspension.

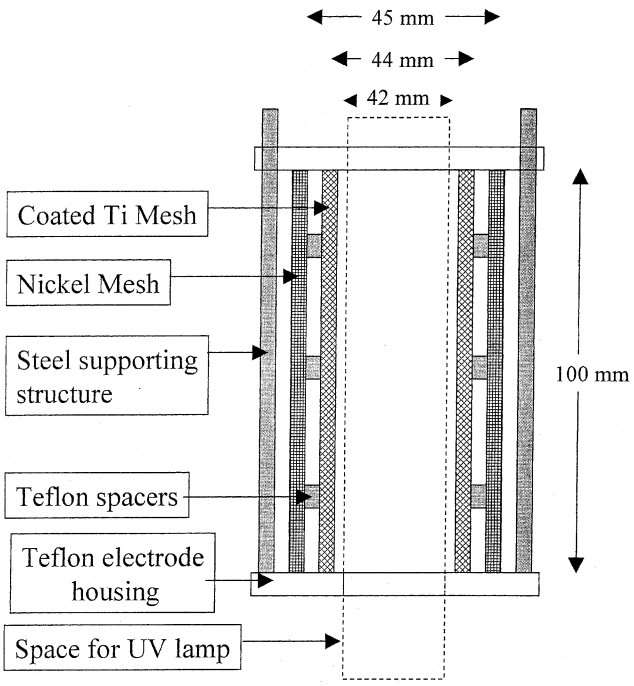


*Fig. 2.* Schematic representation of the electrode 'cassettes' employed in the bubble column reactor.

The anodes used in the reactor were made from the treated titanium mesh, welded along its 10-cm side to form a cylinder (see Figure 2). Nickel mesh (Goodfellow, open area 55%, nominal aperture 0.73 $mm^2$ wire diameter 0.25 mm) was formed into a slightly larger cylindrical counter electrode. The coaxial cylinders were then held in a Teflon housing to form a single 'cassette'. The reactor was used in 2-electrode mode, with all potentials (voltages) quoted with respect to the counter electrode. Figure 2 shows a single 'cassette', two such cassettes were employed in the reactor, as shown in Figure 3. Including the volume above the cassettes and below the outlet arms of the reactor, the volume of solution in the reactor was ca. 1 $dm^3$.

The light source was either two actinic lamps (36 W Philips PL-L) or a 400 W Hg lamp (sharp emission peaks near 365, 405 and 436 nm) axially mounted in the core void. Both lamps have their most intense emission at ca. 436 nm; for comparison purposes only (as neither the anatase nor rutile forms are excited by light of this wavelength) the intensity of the Hg lamp at 436 nm was found to be ca. $10^2\times$ that of the 2 × 36 W lamps. Mineralization per unit charge was very similar for both lamps; however, more mineralization was observed with the Hg lamp, possibly because the relatively greater long-wavelength output of this lamp is less strongly absorbed by the 4-NP.

### 2.3. *Materials and analytical methods*

Titanium tetra-isopropoxide (97%, Aldrich), propan-2-ol (99 + %, Aldrich) and nitric acid (70%, Aldrich) were used as received. Because the aim of the work was to

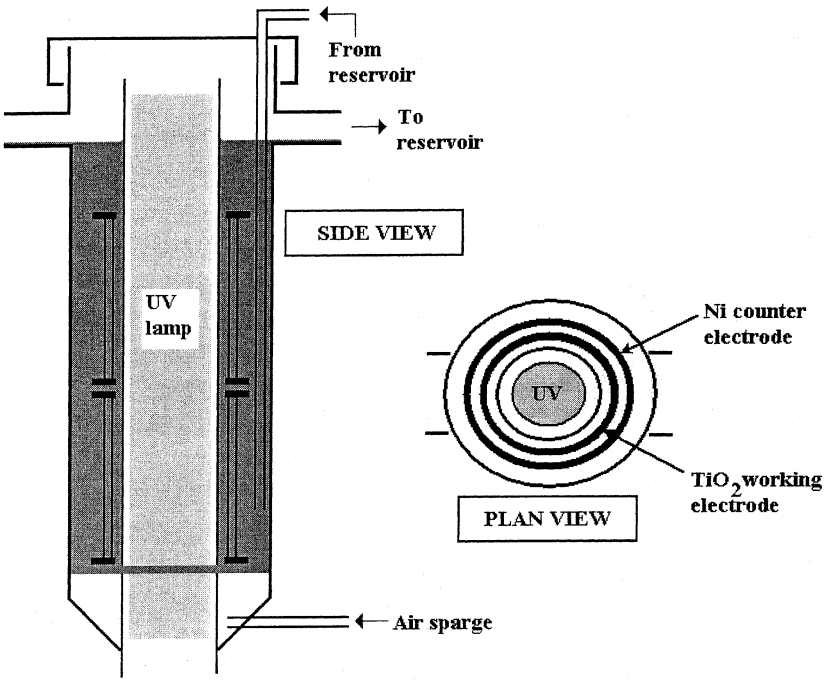


*Fig. 3.* Schematic representation of the bubble column reactor.

treat aqueous waste streams containing NPs, the use of well-defined solutions of analytical grade electrolytes in Millipore water has to be supplemented by measurements in more relevant systems, as in our disinfection studies [18, 19, 23]. Therefore, 0.1 M $Na_2SO_4$ (98%, Aldrich) in Millipore Milli-Q water (18 MΩ cm) and tapwater (Fe < 0.05 mg $dm^{-3}$, $HCO_3^{2-}$ 22 mg $dm^{-3}$, Cu 0.09 mg $dm^{-3}$, Na 13 mg $dm^{-3}$, Mg 5.2 mg $dm^{-3}$, and K 2.9 mg $dm^{-3}$) were used as electrolytes.

HPLC analyses were carried out using Pye Unicam HPLC or Dionex UVD170S HPLC systems, both utilized separation by a Supelco Discovery reverse phase $C_{18}$ column and 40:60:0.001 Methanol (Aldrich, HPLC grade):Milli-Q water:acetic acid (Aldrich). 4-NP was analyzed using its absorption at 320 nm. TOC analyses were measured with a Dohrmann Phoenix 8000 UV/persulphate TOC analyser.

UV–Vis measurements were carried out using a Shimadzu UV–Vis 1201 Spectrophotometer and quartz cuvettes.

## 3. Results and discussion

### 3.1. *Optimization of the photo-anodes*

The thermal $TiO_2$ films were formed on Ti substrates by heating in air [17–19, 23, 24]. Their colours ranged from grey through golden and blue to white, and may be attributed to optical interference [25], a consequence of increasing film thickness as the temperature is raised or heating time increased.

Figure 4(a) shows a typical cyclic voltammogram for a thermal film electrode. A systematic programme to

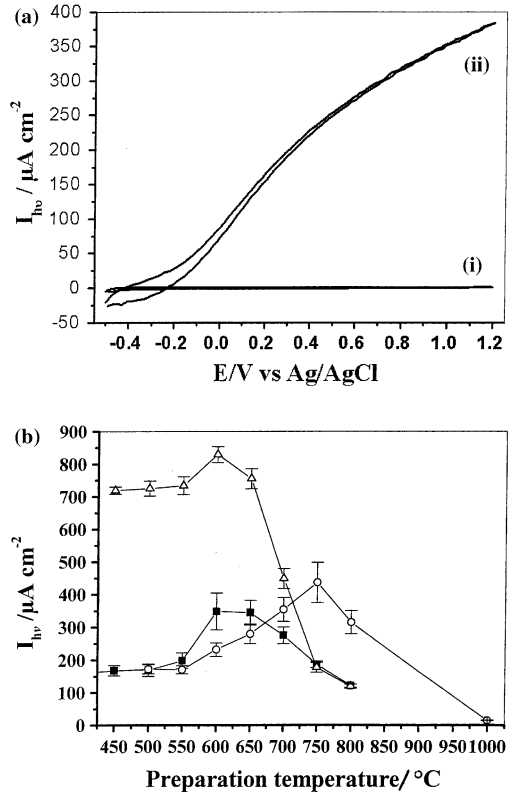


*Fig. 4.* (a) Typical cyclic voltammogram of a 1 × 1 $cm^2$ thermal electrode, prepared at 750 °C, immersed in tap water and irradiated with 2 × 36 W Philips Actinic lamps. Scan rate 100 mV $s^{-1}$. (i) Dark response in both tap water and 1 M methanol; (b) Illuminated response in both tap water and 1 M methanol. (ii) The photocurrent observed at 1.2 V vs. Ag/AgCl as a function of the film fabrication temperature, 1 × 1 $cm^2$ Ti/$TiO_2$ electrode in tapwater, 2 × 36 W Philips Actinic lamps, 100 mV $s^{-1}$. Sol gel electrodes with (Δ) and without (■) 1 M methanol. (○) thermal electrodes.

identify the most effective electrode-fabrication procedure assumed that the photocurrent, measured during cyclic voltammetric runs in tap water, is a direct measure of the rate of production of $^{\cdot}OH$ radicals. Figure 4(b) shows the variation in photocurrent (light–dark current at 1.2 V) for a series of 1 $cm^2$ thermal and sol–gel film electrodes heated at the designated temperature in air for 10 min, removed from the tube furnace and then allowed to cool naturally. The optimum temperature for the thermal films was 750 °C. Neither multiple heating cycles nor longer heating times led to significantly higher photocurrents; in addition, no significant change in the photocurrent was observed if the cyclic voltammetry measurements were made in the presence of 1 M $CH_3OH$.

Figure 5 shows a voltammogram, analogous to that in Figure 4(a), for a sol–gel electrode; in contrast to the behaviour of the thermal $TiO_2$ films, the addition of 1 M methanol resulted in a marked increase in photocurrent. Figure 4(b) shows the variation of the photocurrent with fabrication temperature in the presence and absence of methanol. On the basis of the voltammograms, measured both in the presence and absence of methanol, the optimum preparation exemplified by the 600 °C electrode in Figure 4(b) was identified as ca. 148 g $dm^{-3}$ sol–gel, heated at 600 °C for 10 min. Under similar measurement conditions, the Ineos Chlor electrode gave the highest photocurrent in the presence of 1 M methanol, of 1300 $\mu$A $cm^{-2}$.

### 3.2. *Electrochemical characterization of the photoanodes and the effect of added methanol*

The shapes of the cyclic voltammogramms observed under irradiation very much depend upon electrode type. Those for thermal films, see Figure 4(a), generally conform to the $\sqrt{V}$ dependence of the photocurrent [14] predicted by classical semiconductor theory. The other extreme is typified (Figure 5) by the voltammogramm,

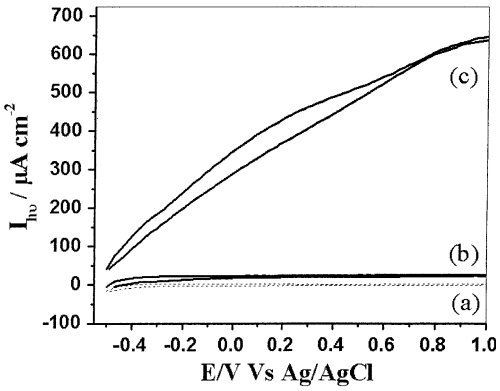


*Fig. 5.* Typical cyclic voltammograms of a sol–gel electrode, spun onto a conducting glass substrate, immersed in tap water and irradiated with 2 × 36 W Philips Actinic lamps with (a) dark response in both tap water and 1 M methanol; (b) illuminated response in tap water; (c) illuminated response in 1 M methanol. Scan rate 100 mV $s^{-1}$.

in the absence of methanol, of the sol–gel film. Here, at potentials ca. 300 mV above onset (i.e. in the region where the theory predicts recombination is not significant) the photocurrent is essentially independent of potential [26]. This behaviour may be interpreted in terms of the model of Vinodgopal et al. [27] who reported laboratory scale studies on the photo *electro*catalytic degradation of organics in aqueous solution with a photoanode of undoped, particulate $TiO_2$ immobilized on a conducting substrate. These authors postulated that the small size of the *undoped* particles resulted in only a very small electric field across each particle which was insufficient to facilitate charge separation. The increase in degradation observed on the application of a potential to the $TiO_2$ electrodes was attributed to increased efficiency of charge separation, caused by both the differing rates of electron and hole transfer at the solution interface (requiring ready access to the interface by hole and electron acceptors, and hence the films to be porous) with a contribution from the potential gradient across the whole film. Jiang and co-workers [26] postulate that diffusion-limited access to the $TiO_2$/water interface by hole and electron acceptors controls photocurrent. Hence, the increased recombination associated with small particles can produce photocurrents which are independent of applied potential and therefore differ markedly from those predicted by classical theory [14].

In our experiments, the exact I/V behaviour shown by a particular particulate $TiO_2$ photoanode could vary anywhere between the two extremes discussed above. However, for the sol–gel and Ineos Chlor films, addition of methanol inevitably led to an increased, and potential-dependent, photocurrent which often showed an approximately linear dependence on $\sqrt{V}$. For the sol–gel electrodes the enhancement was at a maximum at a fabrication temperature up to ca. 600 °C, after which it decreased to zero at ~750 °C, i.e. the range over which anatase converts to rutile.

The effect of dissolved organic on the measured photocurrent from electrophoretically deposited $TiO_2$ electrodes has recently been reported by Jiang and co-workers [26] who also found an increasing photocurrent for an increasing concentration of dissolved organic. They attributed this to direct capture of holes by the adsorbed organic. An earlier, more detailed analysis was reported by Fujishima and co-workers [28] for the specific case of methanol. Fujishima and co-workers interpreted their results in terms of a model in which at low overpotentials (i.e. within ca. 100 mV of the onset of the photocurrent in the absence of added organic) methanol adsorbs on the $TiO_2$ surface and so blocks surface active sites, possibly surface $Ti–O^-$ groups [29] that would otherwise act as recombination centres. Hence methanol can compete effectively with charge recombination and cause an enhanced photocurrent and a lower onset potential (see Figure 5). An alternative proposed mechanism was that the alcohol reduces surface electron–hole recombination by removing

hydroxyl radicals as they form, and hence reduces back donation of electrons. At higher potentials, where surface recombination was postulated to be a less significant factor, due to the high band bending (electric field) in the depletion layer, photocurrent doubling was believed to enhance the photocurrent by direct hole transfer to the alcohol from the valence band, followed by electron injection into the conduction band from the intermediate(s) so formed. Both mechanisms render methanol a probe of, essentially, the 'total oxidizing power' of the $TiO_2$ electrode. The arguments detailed above point to the possibility of surface modification being exploited to differentiate between the two mechanisms, see the work of Park and Choi [30].

### 3.3. *Structural characterization of the photoanodes*

Estimates of the amount of anatase and/or rutile phase and the average crystallite sizes in the various electrodes derived from powder diffraction are presented in Table 1. X-ray diffraction (XRD) showed no discernible crystallinity in thermal films prepared below ca. 650 °C; above this temperature, there was an increasing amount of rutile, reaching ca. 38 wt.% at 850 °C. No anatase was detected at any temperature. The results from all the optimization runs (extended heating time etc.) carried out on the thermal films are plotted in Figure 6 (which includes the data in Figure 4(b)), and clearly show a maximum photocurrent at ca. 22 wt.% rutile. This is the phase composition of the best electrode identified above from the preliminary photocurrent measurements (see Table 1 and Figure 4(b)).

The sol–gel films are more complex. In contrast to the thermal films, anatase was detected in the low-temperature electrodes and increases to a maximum of ca. 6 wt.% at 500–600 °C. The XRD line-broadening indicated a steady growth of anatase crystallites, from 7.5 to 30 nm, as the temperature was increased from 450 to 650 °C. Rutile was detected in the electrodes prepared above 500 °C and increases to 40 wt.% at 800 °C (see Table 1). The smallest rutile crystals were ~30 nm and grew to ~250 nm at 800 °C. Therefore, as the temperature increases and the crystallites grow they convert to rutile. Although massive rutile is thermodynamically stable with respect to anatase at all temperatures, the observed behaviour is consistent with recent calculations [31] which suggest that for very small crystallites the normal stability pattern is reversed, because of the enhanced contribution of the surface.

*Table 1.* Estimated rutile and anatase content, in wt.%, and the crystallite size (nm, in brackets) of the thermal and sol–gel electrodes studied in this paper, see text for details

| Preparation temperature °C | Thermal electrode | | Sol–gel electrode | |
|---|---|---|---|---|
| | Wt.% Anatase | Wt.% Rutile | Wt.% Anatase | Wt.% Rutile |
| 300 | 0 | 0 | | |
| 400 | 0 | 0 | | |
| 450 | | | 4 (7.5) | 0 |
| 500 | 0 | 0 | 6 (10) | 0 |
| 550 | 0 | 0 | | |
| 600 | 0 | 0 | 6 (20) | 4 (30) |
| 650 | 0 | 6 (30) | 5 (30) | 7 (45) |
| 700 | 0 | 15 (50) | 2 (40) | 12 (60) |
| 750 | 0 | 22 (65) | 1 (45) | 27 (150) |
| 800 | 0 | 32 (135) | 0 | 40 (250) |
| 850 | 0 | 38 (270) | | |

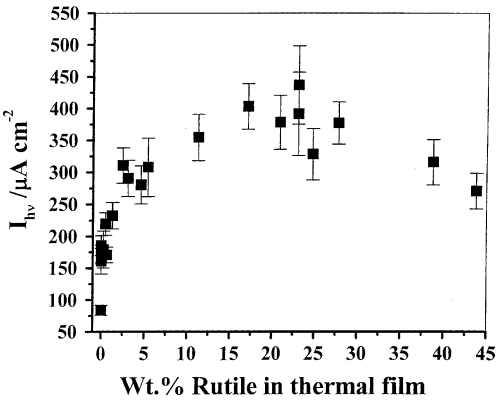


*Fig. 6.* Photocurrent density, measured at 1.2 V vs. Ag/AgCl by cyclic voltammetry (100 mV $s^{-1}$), as a function of the rutile content of the 1 × 1 $cm^2$ thermal $TiO_2$ films. See text for details.

The increase in anatase crystallite size and also, we assume, the amorphous grain size, is predicted to increase the chance of recombination of charge carriers generated deep within a crystal, but in our experiments, the photocurrent observed with both thermal and sol gel films initially increased. This suggest that either the potential gradient is insufficiently developed initially to reduce charge carrier recombination in nanocrystals and/or that even if the applied electric field reduces recombination within the crystal, recombination at the surface, which is of less relative importance in big crystals, is still important. For both types of electrode, the photocurrent in water decreases at high preparation temperatures. The optimum in the current probably results from a balance between the beneficial effects of growth and the detrimental effect of the conversion of amorphous grains (in thermal and sol–gel films) and anatase crystallites (in sol–gel films) to rutile (anatase is generally considered to be more catalytically active than rutile [1, 2]). Since the Vinodgopal model [27] requires relatively high surface area, porous, particulate films that are readily accessible to the electrolyte, we speculate that the photocurrent enhancement on addition of methanol requires both anatase crystallites and porous films and is essentially blocked by rutilization. However, such enhancement has also been seen with single crystal rutile $TiO_2$ and zinc oxide [28].

### 3.4. *Nitrophenol degradation*

The most active sol–gel and thermal electrode fabrication methods identified by the screening process dis-

cussed above were employed to produce mesh electrodes for the BCR, and the degradation of 4-NP, in Millipore water with added 0.1 M $Na_2SO_4$, was investigated.

UV absorption measurements on 4-NP solutions over the concentration range $1 \times 10^{-4}$ to $2 \times 10^{-3}$ mol $dm^{-3}$ showed that at 360 nm, the wavelength of maximum emission from the 36 W lamps, 1 mM 4-NP absorbs 90% of the UV radiation within 2 mm of the lamp-wall of the BCR. As the concentration of 4-NP in the BCR was increased from 0 to 2 mM, there was a steady drop in photocurrent from ca. 100 mA (sol–gel electrode) or 130 mA (thermal mesh electrode) to ~50 mA and this was attributed to reduction, caused by absorption, of the effective intensity of the incident UV light. The photocurrents fell by a factor of ~2.6. This is not consistent with a linear dependence on light intensity, I, as found for example by Jiang et al. [26]; but is entirely consistent with a $\sqrt{I}$ dependence, which suggests significant electron–hole recombination [32, 33], a rather surprising result at the high overpotentials employed. Thus, whilst the results shown in this paper clearly show the positive benefits of the EFE effect, recombination is still important.

Significantly, the Ineos Chlor electrode showed a 33% *increase* in photocurrent (from ca. 135 to ca. 180 mA) on addition of 0.25 mM 4-NP, declining to ca. 105 mA on addition of 2 mM 4-NP. This suggests that on this electrode the initial addition of 4-NP causes current doubling, which is expected to increase with the concentration of organic. At higher concentrations of 4-NP, UV absorption offsets this effect. For this electrode, current doubling dominates at 0.25 mM, and is still significant up to 2 mM 4-NP.

The degradation of 4 $dm^3$ of 0.25-mM 4-NP in 0.1 M $Na_2SO_4$ at the sol–gel mesh electrode is shown in Figure 7(a) and (b); Figure 7(a) shows the loss of 4-NP determined from HPLC measurements, and Figure 7(b) the total organic carbon content of the solution in the reactor as a function of time. A 3-V applied potential does not, without UV, result in any degradation of the 4-NP. Although UV irradiation of the solution in the absence of electrodes results in the apparent degradation of 4-NP (ca. 20% in 11 h), but the unchanged TOC content indicates restricted photochemical conversion to intermediates rather than mineralization to carbon dioxide. Irradiation with the electrode cassettes present but with no applied potential does cause significant *photocatalytic* (as opposed to photo *electro* catalytic) degradation of 4-NP and the amount of degradation is similar for open circuit and short circuit conditions, i.e. approximately 50% of the 4-NP is degraded and 20% mineralized in 500 min. However, if a 1 V potential is applied at the start of irradiation 70% of the 4-NP is degraded and 40% mineralized after 500 min. For 3 V potential the corresponding figures are 95% degraded and 75% mineralized. However, Figure 7(b) shows that increasing the potential from 1 to 3 V doubles the rate of mineralization (corrected for the photochemical contribution) from 0.045 to 0.92 $min^{-1}$, a clear demonstration of electric field enhancement.

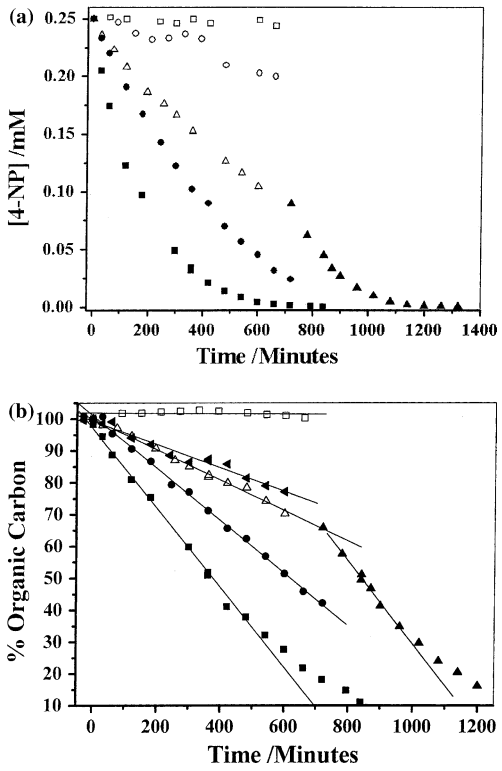


*Fig. 7.* (a) Loss of 4-NP (0.25 mM, 4 $dm^3$ total volume) determined by HPLC ($\lambda = 320$ nm during photoelectrolysis in the BCR using two sol–gel mesh electrode cassettes. (□) Dark, 3 V applied voltage (i.e. between photoanode and counter electrode); (○) No electrode, UV only; (Δ) UV with counter electrode and $TiO_2$ photoanode short-circuited (▲) followed by the simultaneous UV irradiation and application of 3 V : (●)UV, sol–gel electrodes, 1 V applied voltage. (■) UV, sol–gel electrodes, 3 V applied voltage. 400 W Hg lamp. (b) TOC data from the experiments in Figure 7(a). Symbols as in 7(a) except that the 3 V dark and UV only are both represented by □.

Although 0.25-mM 4-NP generated insufficient intermediates to allow their reproducible analyses, at higher concentrations of 4-NP, 4-nitrocatechol, benzoquinone, hydroquinone and 1,2,4-benzenetriol were detected. Similar intermediates have been reported from NP degradation by P25 slurries [20]. A possible mechanism for the degradation of 4-NP at our $TiO_2$ electrodes is shown in Scheme 1. Although 4-NP mineralization is slower than the reduction in concentration of the 4-NP, it is important to note that, after 10 h, 75% of the 4-NP is mineralized in the photoelectrocatalytic experiment. In the absence of applied potential, only 30% is destroyed; the difference is significant in any practical system. Thus, the reactivity sequence is:

*Photoelectrocatalytic* > *Photocatalytic* > *Photochemical* > *Electrochemical.*

The importance of destroying not just starting compounds, but also reaction intermediates was highlighted by the work of Pelizzetti et al. [34], who demonstrated that although the $TiO_2$ slurry photocatalyzed degradation of 25 ppm atrazine was complete within ca. 20 min,

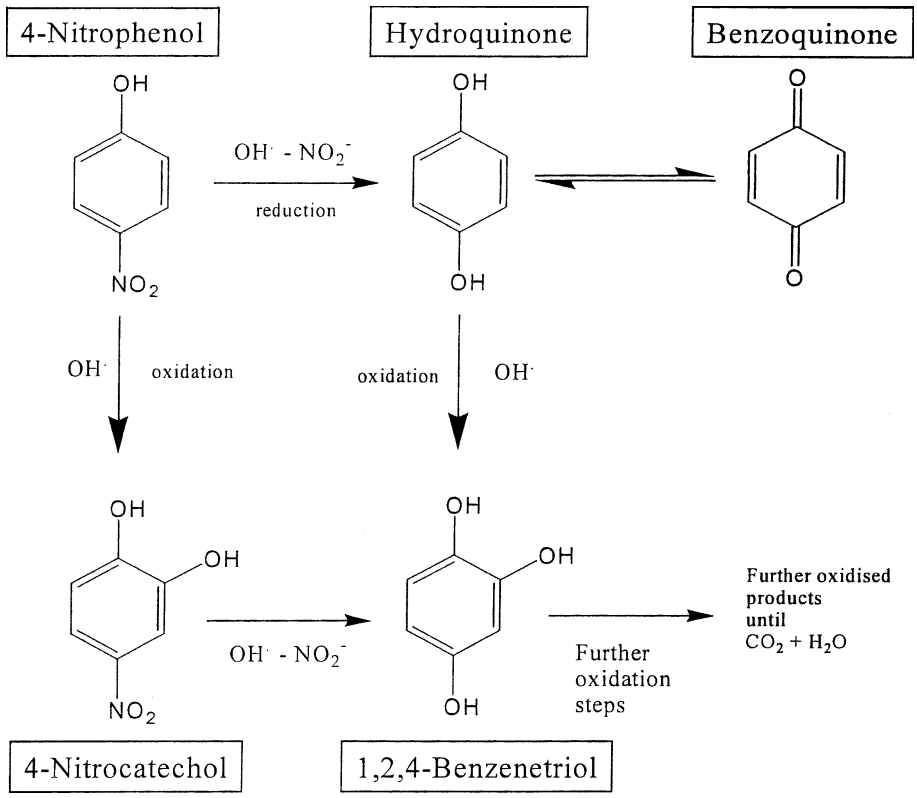


*Scheme 1.* Postulated intermediates in the degradation of 4-NP at an irradiated $TiO_2$ photoanode.

the TOC results only attained a steady state after ca. 120 min, whilst the stoichiometric formation of cyanuric acid, (the final product, rather than $CO_2$ etc) required ~70 h.

The activities of all three electrodes for the degradation of 1.0-mM 4-NP are compared in Figure 8(a) showing the HPLC analyses, and (b) the TOC results. The relative mineralization rates followed the order

Ineos > Sol Gel > Thermal

in both 0.25 and 1.0 mM 4-NP solution. At the higher concentration the increased UV absorption was accompanied by lower (× ca. 5) relative mineralization by sol–gel and thermal electrodes but – because of the current doubling – a much less (×2) relative decrease occurred for the Ineos electrodes. Absolute mineralization rates were much less affected. The difference between the Ineos Chlor electrode and the sol–gel and thermal electrodes is probably the result of current doubling, as discussed in the electrode characterization section. We speculate that the origin of this difference may be related to the porosity/adsorption capacity of the Ineos Chlor electrode facilitating direct electron transfer into photogenerated holes in the valence band which would result in intermediates which can react rapidly at the surface, and are less able to escape into solution than those species participating in the apparently outer sphere reactions at the sol–gel and thermal electrodes. This hypothesis emphasizes the role of structure and surface morphology in determining the detailed mechanism by which organics are oxidized at the irradiated $TiO_2$ surface. However, the role of pores inside the $TiO_2$ film is still uncertain since, when degradation takes place, intermediates may be confined within the pores.

Figure 8(a) and (b) also provide a direct comparison of the photoelectrocatalytic oxidation at immobilized $TiO_2$ electrodes with the photocatalytic degradation and mineralization at the surface of Degussa P25 in suspension. The rutile content of Degussa P25 is ~30% and the surface area is ~55 $m^2\ g^{-1}$; hence, even if all the $TiO_2$ mesh were photoactive with a roughness factor of 10, the surface areas of the mesh electrodes would be ca. 3500× less than that of the slurry. However, in 1 mM solution the activity of the commercial powder was only 2–3 times faster than the commercial electrodes and ~12 times faster than the optimum sol–gel electrode. Mineralization of 0.25 and 1 mM 4-NP by the slurry was complete within 450 min, suggesting that its high surface area and the fact that its particles are continuously swept very close to the UV lamp are responsible for the high activity. The HPLC analyses in Figure 8(a) show that the slurry degrades 90% of the 4-NP within 300 min, whilst the TOC falls by 85% in the same time. Thus, at the P25 surface, intermediates are oxidized equally as rapidly as the 4-NP. At the sol–gel electrode, by contrast, 50% of the 4-NP is lost after 580 min with only 12% decrease in TOC over the same period and neither the sol–gel nor thermal electrodes achieved 50% loss in TOC even after 1200 min irradiation. This again shows that both electrodes show lower activities towards the oxidation

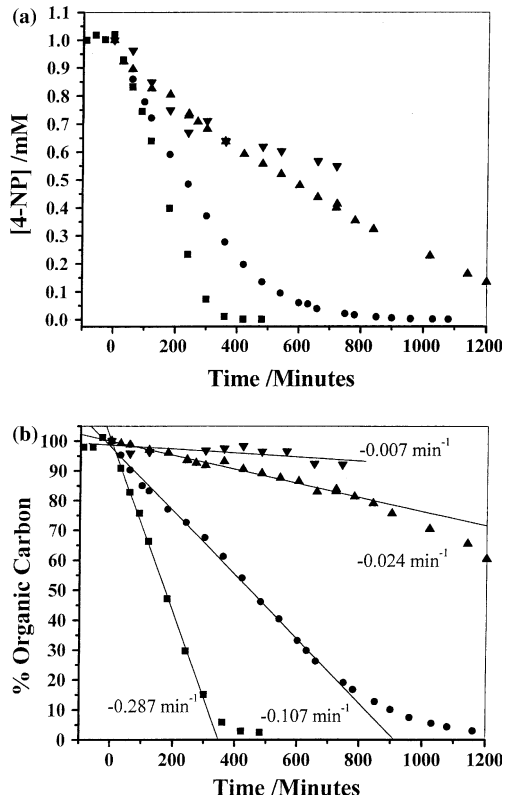


*Fig. 8.* (a) Loss of 4-NP (1.0 mM, 4 $dm^3$ total volume) detected by HPLC ($\lambda = 320$ nm) during photoelectrolysis in the BCR using two mesh electrode cassettes or slurry. (▼) Thermal film, 3 V applied voltage, UV; (▲) sol–gel film, 3 V applied voltage, UV. (◆) Ineos Chlor film, 2 V applied voltage, UV. (■) 4 g $dm^{-3}$ Degussa P25 slurry, UV. 400 W Hg lamp. Slurry only: air-sparge 4 $dm^3$ $min^{-1}$. (b) TOC results from the experiments in Figure 8(a), symbols as 8(a).

of the intermediates produced from 4-NP than towards the reactant itself.

In our study on the mineralization of oxalate [35] the order of catalyst activity was:

$$IneosChlor(7.5) = SolGel(7.5) > slurry(3) > thermal(1)$$

Whilst the activity pattern with respect to the disinfection of water inoculated with *E. coli* [36] was:

$$thermal > sol\text{–}gel > slurry$$

All the above results indicate that the activity of irradiated $TiO_2$ photoanodes towards a particular target species is highly sensitive to the electrode structure and morphology. Further characterization of electrode morphology is therefore in hand.

## 4. Conclusions

This work demonstrates that the photocatalytic oxidation of 4-NP is increased by an applied field and that the effect can be implemented, even for strongly absorbing solutions, at litre scale. In addition, the application of an electric field significantly enhances the mineralization of 4-NP.

Although the oxidation rate in the BCR reactor is not mass-transfer limited – as demonstrated in an earlier paper [18] and confirmed by the different activities of different electrodes – reaction at our best electrode is slower than reaction at the surface of commercial $TiO_2$ particles in suspension. However, despite the limitations imposed by strongly absorbing solutions the rates of oxidation, though slower, are comparable with rates of oxidation by the Degussa P25. This shows that photodegradation by immobilized $TiO_2$ is a worthwhile goal.

Practical achievement of the goal requires more active electrodes. Consequently, catalyst development is a key priority. The effect of methanol on measured photocurrent provides the basis for electrode preliminary classification, but different activity patterns in different reactions show that this optimization must be tailored to the specific reaction. Thus, a comparison of the photoelectrocatalytic oxidation of 2-NP and 4-NP is expected to help elucidate the link between adsorption and catalytic activity since separate measurements (see other paper by same authors in this journal) have demonstrated that adsorption of these two isomers is very different. In this way, understanding of the link between electrode morphology and reaction specificity will be enhanced.

## Acknowledgements

We thank the EPSRC for funding, Huntsman PU and Ineos Chlor for support, and Ineos Chlor for the provision of electrodes. JRT was supported by an EPSRC studentship and SAMK by the Saudi Arabia Ministry of Culture and Science.

## References

1. A. Mills and S. Le Hunte, *J. Photochem. Photobiol. A* **108** (1997) 1.
2. P.A. Christensen and G.M. Walker *Opportunities for the UK in Solar Detoxification*, ETSU s/P4/00249/REP 1996.
3. D.A. Tryk, A. Fujishima and K. Honda, *Electrochim. Acta* **45** (2000) 2363.
4. C.F. Goodeve and J.A. Kitchener, *Trans. Faraday Soc.* **34** (1938) 902.
5. J.H. Carey, J. Lawrence and H.M. Tosine, *Bull. Environ. Contam. Toxicol.* **16** (1976) 697.
6. A.L. Pruden and D.F. Ollis, *J. Catal.* **82** (1983) 404; C.Y. Hsia, C.Y. Lee and D.F. Ollis, *J. Catal.* **82** (1983) 418.
7. T. Matsunaga, R. Tomada, T. Nakajima and H. Wake, *Microbiol. Lett.* **29** (1985) 211.
8. L. Sun and J.R. Bolton, *J. Phys. Chem.* **100** (1996) 4127.
9. T. Torimoto, S. Ito, S. Kiwabata and H. Yoneyama, *Environ. Sci. Technol.* **30** (1996) 1275.
10. W. Choi, J.Y. Ko, H. Park and J.S. Chung, *Appl. Cat. B Environ.* **31** (2001) 209.
11. P. Wyness, J.F. Klausner and D.Y. Goswami, *J. Solar. Eng.* **116** (1994) 8.
12. J.C. Crittenden, Y. Zhang and D.W. Hand, *Water Environ. Res.* **68** (1996) 270.

13. L.M. Peter, *in* R.G. Compton and A. Hamnett (Eds), *Comprehensive Chemical Kinetics*, Vol. 29 (Elsevier, Amsterdam, 1989), p. 353 and references cited therein.
14. A. Hamnett, *in* R.G. Compton (Ed.), *Comprehensive Chemical Kinetics*, Vol. 27 (Elsevier, Amsterdam, 1987), p. 61.
15. J. Gautron, P. Lemasson and J.F. Marucco, *Far. Disc. Chem. Soc.* **70** (1980) 87.
16. H. Gerischer, *Electrochim. Acta* **38** (1993) 3.
17. I.M. Butterfield, P.A. Christensen, A. Hamnett, K.E. Shaw, G.M. Walker, S.A. Walker and C.R. Howarth, *J. Appl. Electrochem.* **27** (1997) 385.
18. J.C. Harper, P.A. Christensen, T.A. Egerton, T.P. Curtis and J. Gunlazuardi, *J. Appl. Electrochem.* **31** (2001) 623.
19. P.A. Christensen, T.P. Curtis, B. Place and G.M. Walker, *Water Res.* **36** (2002) 2410.
20. K.A. Grey, P. Kamat, U. Stafford and M. Dieckmann, *Abstr. Papers Am. Chem. Soc.* **203** (1992) 307-ENVR.
21. B. O'Regan, J. Moser, M. Anderson and M. Gratzel, *J. Phys. Chem.* **94** (1990) 8720.
22. B.D. Cullity, *Elements of X-ray Diffraction* (Addison-Wesley, 1959).
23. J.C. Harper, P.A. Christensen, T.A. Egerton and K. Scott, *Appl. Electrochem.* **31** (2001) 267.
24. T.A. Egerton and P.A. Christensen, *in* S. Parsons (Ed.), '*Advanced Oxidation Processes for Water and Wastewater Treatment*' (IWA Publishing, London, 2004), pp. 167–184.
25. D.L. Douglas and J. Van Landuyt, *Acta Metal.* **14** (1966) 491.
26. D. Jiang, H. Zhao, S. Zhang and R. John, *J. Phys. Chem.* **107** (2003) 12774.
27. K. Vinodgopal, U. Stafford, K.A. Gray and P.V. Kamat, *J. Phys. Chem.* **98** (1994) 6797.
28. O.A. Semenikhin, V.E. Kazarinov, L. Jiang, K. Hashimoto and A. Fujishima, *Langmuir* **15** (1999) 3731.
29. A. Wahl, M. Ulmann, A. Carroy, B. Jermann, M. Dolata, P. Kedzierzawski, C. Chatelain, A. Monnier and J. Augustynski, *J. Electroanal. Chem.* **396** (1995) 41.
30. H. Park and W. Choi, *J. Phys. Chem. B* **108** (2004) 4086.
31. H.Z. Zhang and J.F. Banfield, *J. Mater. Chem.* **8** (1998) 2073.
32. E.A. Salinaro and N. Serpone, *J. Phys. Chem.* **104** (2000) 11202.
33. T.A. Egerton and C.J. King, *J. Oil Col. Chem. Assoc.* **26** (1979) 386.
34. E. Pelizzetti, V. Maurino, C. Minero, V. Carlin, E. Pramauro O. Zerbinati and M.L. Tosato, *Environ. Sci. Technol.* **24** (1990) 1559.
35. J.R. Tinlin, *Ph. D. Thesis*, Newcastle upon Tyne UK (2003).
36. P.A. Christensen, T.P. Curtis, T.A. Egerton, S.A.M. Kosa and J.R. Tinlin, *Appl. Cat. B Environ.* **41** (2003) 371.